
RESEARCH ARTICLE

A machine-learning approach to thunderstorm forecasting through post-processing of simulation data

Kianusch Vahid Yousefnia¹ | Tobias Bölle¹ | Isabella Zöbisch¹ | Thomas Gerz¹

¹Deutsches Zentrum für Luft- und Raumfahrt (DLR), Institut für Physik der Atmosphäre, Oberpfaffenhofen, Germany

Correspondence

Kianusch Vahid Yousefnia, DLR
Oberpfaffenhofen, Institut für Physik der
Atmosphäre, Münchner Str. 20, D-82234
Wessling, Germany
Email: kianusch.vahidyousefnia@dlr.de

Funding information

Internal DLR project DIAL

Thunderstorms pose a major hazard to society and economy, which calls for reliable thunderstorm forecasts. In this work, we introduce SALAMA, a feedforward neural network model for identifying thunderstorm occurrence in numerical weather prediction (NWP) data. The model is trained on convection-resolving ensemble forecasts over Central Europe and lightning observations. Given only a set of pixel-wise input parameters that are extracted from NWP data and related to thunderstorm development, SALAMA infers the probability of thunderstorm occurrence in a reliably calibrated manner. For lead times up to eleven hours, we find a forecast skill superior to classification based only on convective available potential energy. Varying the spatiotemporal criteria by which we associate lightning observations with NWP data, we show that the time scale for skillful thunderstorm predictions increases linearly with the spatial scale of the forecast.

KEYWORDS

thunderstorms / lightning / atmospheric electricity, severe weather, convection, mesoscale, numerical methods and NWP, forecasting (methods), ensembles

1 | INTRODUCTION

While thunderstorms undoubtedly constitute inspiring natural spectacles that move any human being to a certain extent, their impact in the form of lightning, strong winds and heavy precipitation (including hail) is hazardous to society and economy. Besides the small but real chance of being struck by lightning (Holle, 2016), thunderstorms pose a threat to crops and livestock (Holle, 2014) as well, and are known to trigger wild fires (Veraverbeke et al., 2017). In addition, they constitute a major safety concern for aviation (Gerz et al., 2012; Borsky and Unterberger, 2019). Furthermore, thunderstorms and lightning damage electrical infrastructure such as wind turbines (Yasuda et al., 2012), which jeopardizes the transition to sustainable energy production. Finally, since the number of severe thunderstorms is expected to increase due to climate change (Diffenbaugh et al., 2013; Rädler et al., 2019), accurate thunderstorm forecasts become ever more relevant.

Thunderstorm forecasts with lead times of more than one hour usually rely on numerical weather prediction (NWP). This method consists of simulating the future atmospheric state by numerically solving equations derived from the laws of physics. The accuracy of NWP has improved with the advent of high-performance computing, the increased availability of observational data through satellite imagery, as well as advances in data assimilation (Bauer et al., 2015; Yano et al., 2018). In order to use NWP data for thunderstorm predictions, one needs to know how thunderstorms manifest themselves in terms of the NWP output fields. In a post-processing step, this knowledge is then used to identify signs of thunderstorm occurrence in simulation data.

Various ideas for identifying signs of thunderstorm occurrence have been put forward in recent years. For instance, post-processing of NWP data has been blended with now-casting methods (Kober et al., 2012; Hwang et al., 2015). Empirical knowledge on convective activity has been translated into expert systems using fuzzy logic (Lin et al., 2012; Li et al., 2021). The fuzzy logic technique allows the construction of decision rules for thunderstorm occurrence based on domain knowledge. Lately, machine learning (ML) methods based on artificial neural networks have gained popularity. These methods generalize the fuzzy logic approach in the sense that decision rules are constructed by solving a data-

driven optimization problem. Works include neural networks with relatively few neurons (Ukkonen and Mäkelä, 2019; Jardines et al., 2021; Kamangir et al., 2020), as well as deep neural networks with convolutional layers and millions of trainable parameters (Geng et al., 2021; Zhou et al., 2022). Findings suggest that neural network models are more skillful at predicting thunderstorm occurrence than comparable ML approaches like random forests (Ukkonen and Mäkelä, 2019).

The promising results in ML have encouraged us to apply neural network methods to historical simulation data of ICON-D2-EPS, an NWP ensemble model for Central Europe with a horizontal resolution of ca. 2 km (Zängl et al., 2015; Reinert et al., 2020). ICON-D2-EPS is a limited-area model which explicitly resolves convection and is run operationally by the German Meteorological Service (DWD). To the best of our knowledge, neural networks have not yet been employed for the identification of thunderstorm occurrence in ensemble data with a comparable horizontal resolution. In this work, we present the neural network model SALAMA (Signature-based Approach of identifying Lightning Activity using Machine learning). It has been trained to predict thunderstorm occurrence through the post-processing of simulation data. In section 2, we describe how independent datasets for the training, testing and validation of our model have been compiled from NWP forecasts and lightning data. Details on the ML architecture are provided in section 3. While thunderstorm occurrence is identified in a pixel-wise manner, we systematically vary the spatiotemporal criteria by which the lightning observations are associated with the NWP data. This enables us to study the effect of different spatial scales on the model identification skill and allows us to estimate the advection speed of thunderstorms. Further results are presented in section 4 and demonstrate that, for lead times up to at least eleven hours, SALAMA is more skillful than a baseline method based only on convective available potential energy. In addition, we show a linear relationship between the spatial resolution scale of our model and the time scale during which skill decreases with lead time. This is consistent with earlier findings that resolving smaller scales brings faster growing forecast errors about (Lorenz, 1969; Selz and Craig, 2015).

2 | DATA

We collected simulation data from the ICON-D2-EPS ensemble model, as well as lightning observations from the lightning detection network LINET (Betz et al., 2009). The simulations were used to extract predictors of thunderstorm occurrence. The lightning observations serve as ground truth. The model domain of ICON-D2-EPS covers the areas of Germany, Switzerland, Austria, Denmark, Belgium, the Netherlands and parts of the neighboring countries. For our study, we cropped the model domain at its borders by approximately 100 km to reduce boundary computation errors, which yielded the study region given in fig. 1. In a cylindrical projection, it corresponds to a rectangle with the southwest corner located at 45°N, 1°E, the northeast corner located at 56°N, 16°E and all sides being either parallels or meridians. There are daily model runs every three hours starting at 00 UTC, with 20 ensemble members per run. We collected simulation data from June to August 2021 over the entire domain in fig. 1 in hourly steps, taking always the latest available forecast for each hour. Following this procedure results in forecasts with lead times of 0 h, 1 h or 2 h.

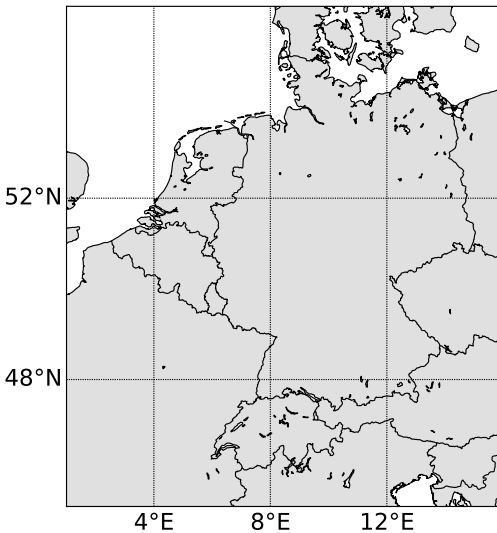


FIGURE 1 Map of the study region.

2.1 | NWP predictors

The atmospheric fields used as predictors of thunderstorm occurrence in this study are given in table 1. They have been selected as follows: We considered as candidate predictors all two-dimensional fields provided in ICON-D2-EPS, as well as two ICON-D2-EPS pressure-level fields associated with deep moist convection in the literature, namely the relative humidity at 700 hPa and the vertical wind speed in pressure coordinates at 500 hPa (Li et al., 2021). In addition, we stipulated that the predictors be available on the open-data server of the DWD (<https://opendata.dwd.de>, last visit: 2023-03-14), such that the trained model can eventually be used in real-time. For a given candidate input field, we retrieved values on the grid points and time instants on the study domain and period. We also checked for each value whether a thunderstorm occurred (cf. section 2.2). Next, we compared histograms of the distribution of the given field during and in the absence of thunderstorm occurrence and kept only fields that differed significantly in the two distributions.

As shown in table 1, all predictors can be related to thunderstorm activity through physical mechanisms like instability and moisture. In particular, our selection process has led to predictors that agree with findings in the literature (Ukkonen and Mäkelä, 2019; Jardines et al., 2021; Leinonen et al., 2022). Conversely, convective inhibition (CIN), which is sometimes listed as a convective predictor (Kamangir et al., 2020), has not passed the selection process. This is likely due to the fact that we have checked for predictive power in terms of developed thunderstorms. CIN, however, correlates with the hours leading up to a thunderstorm and has been removed once the storm reaches its mature stage.

It is worth stressing that we have excluded certain parameters on purpose, namely the geographical location of a thunderstorm event, the time of the day, and the time of the year. In doing so, we assume the existence of a universal signature shared by all thunderstorms, irrespectively of where and when they occur. In addition, the list of predictors does not include the lead time of the forecast. We check in section 4 whether our model, which has been trained on data with lead times between 0 h and 2 h, displays skill on data with longer lead times.

TABLE 1 List of the 21 input parameters used in the study ("DIA": including sub-grid scale).

physical significance	ICON parameter name	description
instability	CAPE_ML	mixed-layer convective available potential energy
	CEILING	ceiling height
	OMEGA500	vertical wind speed in pressure coordinates at 500 hPa
	PS	surface pressure
	PMSL	surface pressure reduced to mean sea level
cloud cover	CLCH	high level clouds (0-400 hPa)
	CLCM	mid-level clouds (400-800 hPa)
	CLCL	low-level clouds (800 hPa to soil)
	CLCT	total cloud cover
precipitation and moisture	DBZ_CMAX	maximal radar reflectivity
	ECHOTOP	echotop pressure
	RELHUM700	relative humidity at 700 hPa
	RELHUM_2M	2 m relative humidity
column-integrated	TQC, TQC_DIA	cloud water
water quantities	TQG	graupel
	TQI, TQI_DIA	ice
	TQV, TQV_DIA	water vapor
	TWATER	total water content

2.2 | Lightning observations

In supervised learning, ML models are trained on data for which the ground truth is known. For this reason, we required knowledge of thunderstorm occurrence for our study domain and period. By reason of their high detection efficiency and spatial accuracy over the entire study region, we employed lightning observations to assess the occurrence of thunderstorms. Specifically, we resorted to the LINET network (Betz et al., 2009), which exploits the radio spectrum to continuously measure strokes of lightning over Europe. The technology achieves a detection efficiency of more than 95 % and an average location accuracy of 150 m. While the technology is able to differentiate between cloud-to-ground and intracloud flashes, we have considered all lightning events as we are only interested in the yes/no occurrence of thunderstorm activity.

Given a set of predictors retrieved from a grid point x on the study domain at time t during the study period, we considered thunderstorm activity to occur at (x, t) if a flash

was detected at any (x_l, t_l) with

$$\|x - x_l\| < \Delta r \quad |t - t_l| < \Delta t, \quad (1)$$

where $\|\cdot\|$ denotes the great-circle distance between x and x_l . We trained our model with different values for the spatial and temporal thresholds Δr and Δt in order to study the relationship between them and classification skill systematically.

2.3 | Compiling independent data sets

The data obtained from NWP and lightning observations can be considered a set of tuples (ξ, y) , where $\xi \in \mathbb{R}^n$ denotes the $n = 21$ input parameters and $y \in \{0, 1\}$ corresponds to a label of the ground truth (1: thunderstorm occurrence, 0: no thunderstorm occurrence). As the input fields were provided on a triangular grid, we first performed an interpolation onto a $0.125^\circ \times 0.125^\circ$ longitude/latitude grid. The labels were produced on the same grid. For each full hour during the study period, for each ensemble member and for each grid point, we fetched the input parameters and the corresponding

label, taking always the latest available forecast.

We compiled three statistically independent data sets: The training set is used only for training the neural network model (a precise definition of training is given in section 3.1), while its skill is measured on a test set with data that the model has not seen during training. A third data set, the validation set, is used to monitor training progress (cf. section 3.1). In an attempt to assure statistical independence between the data sets, we took two measures. First, assuming possible day-to-day correlations in the input parameters (e.g. induced by the synoptic scale) to be negligible for convective events with life spans of the order of a few hours, we used separate days for training, testing and validation. In addition, we took into account that intense thunderstorms that form in the afternoon may well live on after 0 UTC. We therefore defined days to begin at 8 UTC, a time of the day chosen by checking when lightning activity in the collected data is minimal. The latter measure prevents data from one thunderstorm at different times to appear in separate data sets.

Figure 2 offers an overview of the days contained in each data set. The days were randomly distributed among the three sets. Furthermore, we have randomly subsampled the sets such that the training set consists of 4×10^5 tuples, and the test and validation sets each contain 10^5 tuples. The subsampling has been performed in a manner that the training set is class-balanced (both labels appear equally frequently), while no correction to imbalance has been done for the test and validation sets. The reason for this correction was to prevent the model from learning to simply predict the majority class at all times. This correction, however, requires additional care, which is discussed in section 3.2.

3 | METHODS

In this section, we provide details on SALAMA, focusing on how it has been trained and calibrated. In addition, we introduce metrics for the evaluation of model skill and present a baseline model for comparison.

1	2	3	4	5	6	7	8	9	10	11
12	13	14	15	16	17	18	19	20	21	22
23	24	25	26	27	28	29	30	June		
1	2	3	4	5	6	7	8	9	10	11
12	13	14	15	16	17	18	19	20	21	22
23	24	25	26	27	28	29	30	31	July	
1	2	3	4	5	6	7	8	9	10	11
12	13	14	15	16	17	18	19	20	21	22
23	24	25	26	27	28	29	30	August		

FIGURE 2 Days (from 8 UTC to 8 UTC) during the summer of 2021 which were used for compiling the datasets for training (dark brown), testing (light blue with bold numerals) and validation (light green). The days have been distributed at random among the three sets.

3.1 | Model description

It is worthwhile to introduce some ML terminology. The three data sets used for training, testing and validation (cf. section 2.3) are made up of examples (ξ, y) . Each example consists of a pattern $\xi \in \mathbb{R}^n$ of n input features and a label $y \in \{0, 1\}$.

Given a pattern ξ , the problem at hand is to infer the probability of thunderstorm occurrence, which constitutes a task known as binary classification. In the following, we consider both the pattern and its corresponding label to originate from a random experiment. Therefore, let Ξ be an n -dimensional random variable for the pattern and let Y be a random variable of thunderstorm occurrence (1: thunderstorm, 0: no thunderstorm). We are interested in $P(Y = 1 | \Xi = \xi)$, namely the conditional probability of thunderstorm occurrence if the pattern is known. A feedforward artificial neural network model is a function $f : \mathbb{R}^n \rightarrow (0, 1)$ that models the relationship between the input pattern and the corresponding probability of thunderstorm occurrence. We refer to f simply as neural network. Neural networks use compositions of matrix multiplications, as well as non-linear operations referred to as activation functions. The architecture of our neural network is presented in fig. 3: It consists of the input and output layer as well as hidden layers, where each layer is a vector of numbers

obtained from the previous layer by one matrix multiplication and by applying an activation function to the result in a component-wise manner. The complexity of f is adjustable through the number of hidden layers and the size of each hidden layer, i.e. the number of nodes. Our model has three hidden layers and 20 nodes per hidden layer. Moreover, we use rectified linear units for the hidden layers and a sigmoid function to map the output layer to a probability between zero and one.

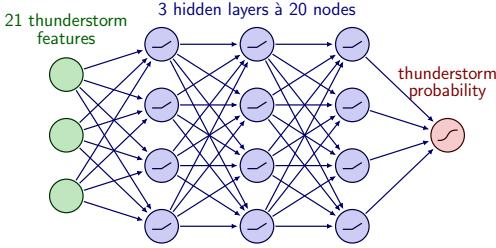


FIGURE 3 (Color online) The architecture of SALAMA: Input features are scaled to order 1. We use rectified linear units as activation functions in the hidden layers. A sigmoid function maps the output layer to the open interval $(0, 1)$.

The entries, also referred to as weights, of the matrices that connect the layers are adjusted according to the data in the training set. We therefore add a subscript $w \in \mathbb{R}^d$ to f to express the dependence on the d weights. If f_w constitutes an accurate representation of the conditional probability of thunderstorm occurrence, i.e. $f_w(\xi) \approx P(Y = 1 | \Xi = \xi)$, then the likelihood of observing a label y for a given input feature ξ reads

$$L(w|\xi, y) = \begin{cases} f_w(\xi), & y = 1 \\ 1 - f_w(\xi), & y = 0 \end{cases} \quad (2)$$

Denote by $(\xi^{(i)}, y^{(i)})_{i=1 \dots N}$ the training set with N examples. The most likely configuration of weights, given the training set, is then obtained by minimizing the negative logarithm of the likelihood function,

$$-\log \mathcal{L}(w) = - \sum_{i=1}^N \log L(w|\xi^{(i)}, y^{(i)}), \quad (3)$$

with respect to the weights. The expression in eq. (3) is referred to as binary cross-entropy loss function in ML terminology. The process of determining the weights that minimize loss is called training. We trained SALAMA using the robust iterative stochastic method Adam (Kingma and Ba, 2014). However, if one used the configuration of weights which minimizes eq. (3) exactly, a neural network would likely suffer from overfitting, i.e. learning parts of the noise in the data as well. To this end, we implemented an early stopping procedure, in which loss was monitored on the validation set during training. Once the validation loss no longer decreased, training was stopped.

Before training, each input feature has been scaled in a way that its sample standard deviation in the training set is of the order of unity. In addition, we trained not only on the architecture presented in fig. 3 but also varied the number of hidden layers, as well as the number of nodes per layer. We found that once a certain complexity was reached in terms of the size of the network, adding new nodes or layers had no effect on the validation loss at the end of training. The architecture in fig. 3 constitutes the smallest network for which this complexity threshold has been exceeded.

3.2 | Model reliability

As described in section 2.3, we have artificially increased the fraction of positive examples in the data set used for the training of our neural network. It is crucial to understand that if the trained model were naively applied to a test set with a different fraction of positive examples, it would produce probabilities that are inconsistent with the observed relative frequency of thunderstorm occurrence.

In order to see this, we use Bayes' theorem to expand the conditional probability of thunderstorm occurrence given a pattern ξ , which yields:

$$P(Y = 1 | \Xi = \xi) = \frac{P(\Xi = \xi | Y = 1)P(Y = 1)}{P(\Xi = \xi)}. \quad (4)$$

The denominator can be expressed as

$$P(\Xi = \xi) = P(\Xi = \xi | Y = 1)P(Y = 1) + P(\Xi = \xi | Y = 0)P(Y = 0). \quad (5)$$

Let $P(Y = 1) = 1 - P(Y = 0) = g$, where g denotes the climatological probability of thunderstorm occurrence with no prior knowledge. Then,

$$P(Y = 1|\Xi = \xi) = \frac{1}{1 + (1 - g)R(\xi)/g}, \quad (6)$$

where the residual function $R(\xi) = P(\Xi = \xi|Y = 0)/P(\Xi = \xi|Y = 1)$ is not expected to depend on g . Equation (6) shows that the conditional probability of thunderstorm occurrence carries an implicit g -dependence. Now remember that the training set contains an increased fraction $\tilde{g} = 1/2$ of positive examples, while the corresponding fraction in the test set is (up to fluctuations due to the finite sample size) equal to the climatological value g . During training, the neural network, therefore, learns to produce the following model output

$$f_w(\xi, \tilde{g}) = \frac{1}{1 + (1 - \tilde{g})R(\xi)/\tilde{g}}. \quad (7)$$

When we want to apply our neural network to a dataset with $g \neq \tilde{g}$, the correct probability output reads

$$f_w(\xi, g) = \frac{f_w(\xi, \tilde{g})}{f_w(\xi, \tilde{g}) + \frac{1-\tilde{g}}{g} \frac{\tilde{g}}{1-\tilde{g}} (1 - f_w(\xi, \tilde{g}))}, \quad (8)$$

which can be derived by formulating eq. (7) with g and \tilde{g} and substituting one equation into the other one.

If the model probability output is consistent with the observed relative frequency of thunderstorm occurrence, the model forecasts are referred to as reliable. In order to check whether our neural network provides reliable forecasts, we used the test set to produce a reliability diagram. For this purpose, one partitions the interval $(0, 1)$ of possible forecast probabilities into bins. For each bin, one considers all examples whose model probability falls into the bin. Then, one computes the relative frequency of thunderstorm occurrence and plots it against the average model probability per bin. An example for one configuration of lightning labels is shown in fig. 4, for which 10 equidistant bins have been used. The uncertainty on the observed frequency spans the 5th and 95th percentiles of fluctuations and has been estimated through a bootstrap resampling procedure similar to Bröcker and Smith (2007): By drawing with replacement, one produces variations of the original test set and considers the

sample-to-sample fluctuations of observed relative frequencies. While producing reliable forecasts for probabilities close to 0 and 1, our model underestimates the relative frequency of thunderstorm occurrence for forecast probabilities below 0.7. Further calibration could be done using statistical methods like isotonic regression (Niculescu-Mizil and Caruana, 2005), which is beyond the scope of this work. Instead, we consider our model sufficiently reliable and appreciate that the level of reliability has been attained by means of the analytical correction (8) alone.

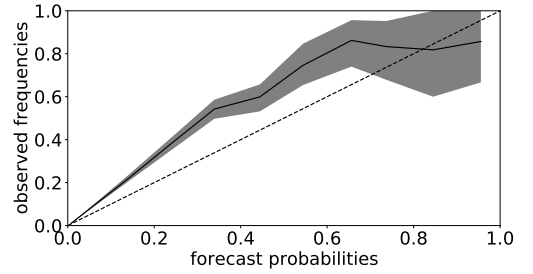


FIGURE 4 Observed relative frequency of thunderstorm occurrence as a function of model output probability, evaluated for the test set with the label configuration $\Delta r = 15$ km, $\Delta t = 30$ min (cf. section 2.2). Line thickness corresponds to the symmetric 90 % confidence interval obtained by bootstrapping 200 resamples, see text for details. The dashed 1:1 line corresponds to a model with perfect reliability.

3.3 | Skill evaluation metrics

While the neural network outputs a continuous probability p , many metrics for evaluating classification skill require a conversion from probability into binary output. This is done by introducing a decision threshold \tilde{p} . If $p > \tilde{p}$, thunderstorm occurrence for the corresponding example is deemed "true", otherwise "false". In combination with the two options from the label, there are four possible outcomes for each example. They are presented as a contingency matrix in table 2. Given a test set and a fixed decision threshold, the probability of

TABLE 2 Contingency matrix for binary classification.

		observed thunderstorm	
		true	false
forecast thunderstorm	true	hit	false alarm
	false	miss	correct reject

detection (POD) and false-alarm ratio (FAR) are defined by

$$\text{POD} = \frac{\text{hits}}{\text{hits} + \text{misses}}, \quad (9)$$

$$\text{FAR} = \frac{\text{false alarms}}{\text{hits} + \text{false alarms}}. \quad (10)$$

Here, "hits" refers to the number of examples in the test set that qualify as "hit" according to table 2.

3.4 | Baseline model

Mixed-layer convective available potential energy (CAPE) is a measure of atmospheric instability and a necessary condition for deep moist convection (Markowski and Richardson, 2011; Ukkonen and Mäkelä, 2019). We implemented a simple baseline model which forecasts a thunderstorm if CAPE exceeds a fixed decision threshold. Although this baseline approach does not explicitly involve thunderstorm probabilities, its skill can be nevertheless quantified by the scores introduced in section 3.3. The contingency matrix elements in table 2 adapt straightforwardly. For instance, an example in a test set is referred to as a "hit" if a positive lightning label coincides with CAPE exceeding the decision threshold.

4 | RESULTS

Having trained SALAMA, we can straightforwardly post-process ensemble data with it. For example, if we have, for a given location, a 3 h-forecast of ICON-D2-EPS at hand, it consists of 20 input feature tuples (one tuple for each ensemble member). One can now compute a thunderstorm probability according to eq. (8) for each member. As we will discuss in section 4.2, the ensemble spread of thunderstorm probability is linked to the model uncertainty of the input features. In the following, we compare SALAMA to the baseline model

based on CAPE (cf. section 3.4) and move on to investigating how the spatiotemporal thresholds of the lightning label configuration (cf. section 2.2) influence the classification skill of SALAMA as a function of lead time.

4.1 | Comparison to baseline model

We keep the thresholds of the lightning label configuration (cf. section 2.2) fixed to the particular choice $\Delta r = 15$ km, $\Delta t = 30$ min in this section. The climatological fraction of thunderstorm examples in the test set amounts to $g = 0.021$ in this configuration. The results, however, do not change qualitatively if another configuration is used.

In fig. 5, we run SALAMA for three consecutive hours of an evening with thunderstorm occurrence over Southern Germany. More precisely, we plot the ensemble-averaged probability of thunderstorm occurrence for the entire study domain on a map. Pixels with observed thunderstorm occurrence are colored in as well. For a comparison to the baseline model, we add a row of plots which show the spatial distribution of ensemble-averaged mixed-layer CAPE. For both models, we compute POD and FAR based on the map pixels. The decision threshold used for their computation (cf. section 3.3) is chosen for each model such that forecasts are unbiased. This means that the average fraction of examples classified as thunderstorms is equal to the observed fraction of thunderstorm examples. The threshold found for CAPE is supported by previous findings (Zöbisch et al., 2020). The color bar is prepared such that probabilities above the decision threshold are marked with a significantly darker color than probabilities below it. For this example case, one can see immediately that SALAMA detects thunderstorm occurrence more reliably than the baseline model (which we simply call CAPE in the following), while at the same time providing fewer false alarms. Note that this particular day has not been used for the training of SALAMA.

In order to demonstrate that the difference in skill is not specific to the particular evening displayed in fig. 5 but generalizes to the entire study period, we compute skill scores for the test set introduced in section 2.3, which consists of examples of the entire summer of 2021. POD and FAR depend on the decision threshold used to convert probabilities (or CAPE values) to binary output (cf. section 3.3). Drawing

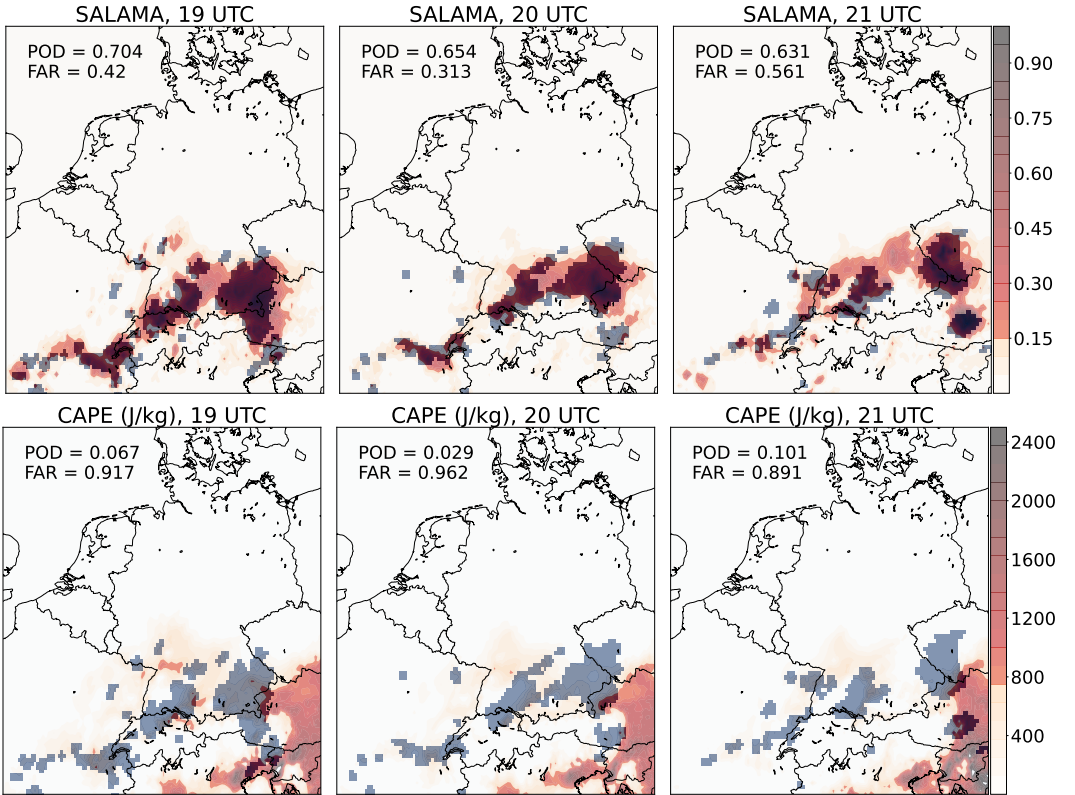


FIGURE 5 (Color online) Upper row: probability of thunderstorm occurrence (red) for SALAMA on June 23, 2021 from 19 UTC on. The model lead times for the three hours are 1 h, 2 h, and 0 h, respectively. Displayed is an average over 20 ensemble members. Lightning labels ($\Delta r = 15$ km, $\Delta t = 30$ min, cf. section 2.2) in blue. Lower row: ensemble-averaged mixed-layer CAPE (red) and lightning labels (blue). We have introduced a jump in the color maps to show the decision thresholds. The thresholds (SALAMA: 14.8 %, CAPE: 763 J kg^{-1}) are chosen such that the models are unbiased.

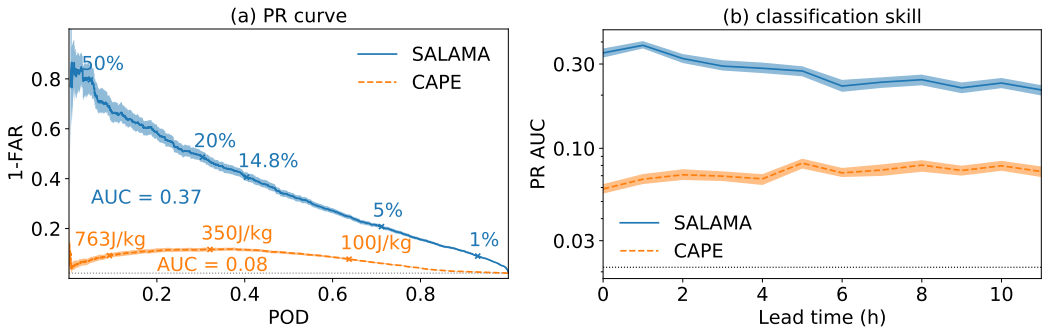


FIGURE 6 (Color online) (a) PR curve for SALAMA (solid) and the CAPE-based model (dashed), evaluated on the test set. The annotations added to the curves correspond to different decision thresholds, cf. section 3.3 (b) Classification skill (quantified by the area under the PR curve) as a function of lead time. In both figures, grey dotted lines denote models with no identification skill. Uncertainties are obtained from 200 bootstrap resamples and show the symmetric 90 % confidence interval.

(POD, $1 - \text{FAR}$) for different decision thresholds into one diagram, one obtains the curve shown on the left-hand side of fig. 6. It is referred to as precision-recall (PR) diagram and is used to evaluate the classification skill of a model. A random model with no skill corresponds to the dashed horizontal curve $1 - \text{FAR} = g$, where g denotes the climatological fraction of positive examples in the test set. Models with skill display PR curves above the horizontal line, with higher areas under the curve (AUC) indicating higher classification skill. The uncertainties are computed here, as well as for the remaining figures in this section, by the bootstrap resampling method introduced in section 3.2. The models which are considered here display higher skill than a random model following climatology would. SALAMA, however, has higher classification skill than CAPE, as can be seen from the higher AUC in the PR curve in fig. 6. This illustrates that a multi-parameter approach to thunderstorm forecasting is superior to employing a single input feature.

With this quantitative analysis at hand, a couple of comments are in order. Firstly, the PR curve of CAPE increases for $\text{POD} \lesssim 0.39$, which suggests that the visual overlap between the CAPE output and the labels in fig. 5 could be slightly increased by choosing a lower decision threshold. This, however, would cause the model to become biased towards predicting too many thunderstorms. Secondly, the decision threshold used for SALAMA in fig. 5 corresponds to a point with $\text{POD} = 1 - \text{FAR} \approx 0.40$, which means that the skill which

SALAMA displays in fig. 5 is above the average skill during the summer of 2021. Thirdly, it is worth appreciating that the PR curves of SALAMA and CAPE can be directly compared to each other even though they are parameterized differently (probabilities vs. CAPE values). The mathematical reason for this is that the shape of a parametrized curve, as well as the area under its curve, is invariant under reparametrizations. There is a crucial implication to this, which concerns the reliability diagram of SALAMA (cf. fig. 4): Even if we included a further calibration step to increase reliability, this would actually have no effect on the classification skill measured by the area under the PR curve.

4.2 | Lead time dependence of classification skill

In the remainder of this section, we investigate how the classification skill of SALAMA depends on the lead time of the NWP forecast from which the input features originate. For this purpose, we generate test sets in which the examples come from NWP forecasts with fixed lead time. Each set contains 10^5 examples. We use the same dates as for the test sets introduced in section 2.3. On the right-hand side of fig. 6, we plot the SALAMA classification skill, measured in terms of the area under the PR curve, as a function of lead time and compare it to the dependence obtained for CAPE. The figure shows that, for SALAMA, classification skill decreases ap-

proximately exponentially (note the log-scaling of the y-axis) for lead times longer than 1 h, while the corresponding curve for CAPE remains nearly constant for all lead times considered here. Nevertheless, even for 11 h forecasts, SALAMA remains more skillful than any forecast using CAPE. The classification skill of SALAMA at a lead time of 1 h is actually higher than at 0 h. This is likely a spin-up effect resulting from the NWP model (Sun et al., 2014).

It is tempting to assume that the decrease in skill with lead time originates from an increasing NWP forecast uncertainty for longer lead times. We can use ensemble data to check this hypothesis. Let q be either one of the 21 input features or the model thunderstorm probability, i.e. a quantity that is given for each ensemble member and for all lead times. Then define the ensemble spread σ'_q of q as the ensemble standard deviation of q ,

$$\sigma'_q(t_{\text{lead}}) = \sqrt{\langle q(t_{\text{lead}})^2 \rangle - \langle q(t_{\text{lead}}) \rangle^2}, \quad (11)$$

where we make the dependence on the lead time t_{lead} explicit. The brackets $\langle \cdot \rangle$ denote the average over all 20 ensemble members. Denote by $\overline{\sigma'_q}(t_{\text{lead}})$ the expression obtained by performing an average of σ'_q over the entire study region and all times associated with the test set. Lastly, we define the normalized ensemble spread of q ,

$$\sigma_q(t_{\text{lead}}) = \frac{\overline{\sigma'_q}(t_{\text{lead}})}{\overline{\sigma'_q}(0 \text{ h})}, \quad (12)$$

as a function of lead time. It quantifies ensemble spread in such a way that different input features can be directly compared to each other. In fig. 7, the normalized ensemble spread of each of the 21 input features is shown as thin solid lines and the corresponding curve for the model output of SALAMA is drawn in thick and dashed. One can see that the ensemble spread does indeed increase with lead time for most input features, the increase being approximately linear. The ensemble spread of the SALAMA output increases in line with the majority of the input features and with a similar slope. This suggests that the decrease in classification skill observed in fig. 6 is solely due to the increasing variance in the simulation data.

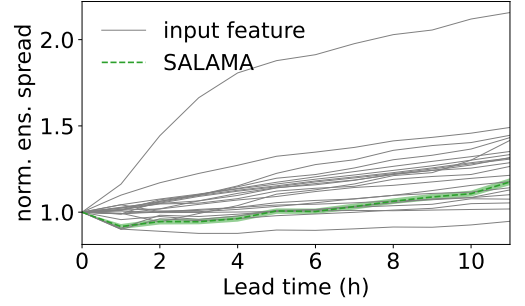


FIGURE 7 Normalized ensemble spread (cf. eq. (12)) of input features in comparison to spread of model thunderstorm probability as a function of lead time. Each thin solid line refers to one of the 21 input features. The thick dashed green line is associated with SALAMA probability output. Its line thickness represents the symmetric 90 % confidence interval of uncertainty, estimated with 200 bootstrap resamples.

4.3 | Effect of the label size

So far, the temporal and spatial thresholds, Δr and Δt , of the label configuration have been fixed. In this section, we study their effect on the classification skill of SALAMA. As a first step, we compute the area under the PR curve for several label configurations, which is shown in fig. 8. The color pattern in the figure suggests that the two thresholds are not independent variables of classification skill. Instead, one can find a parameter c with the units of a velocity such that classification skill is nearly constant along lines

$$s = \Delta r + c \Delta t = \text{const.} \quad (13)$$

Indeed, s corresponds to a spatial resolution scale; it determines the minimal spatial accuracy that can be expected from a model trained with a given label configuration. We expect the parameter c to roughly quantify the speed at which regions of thunderstorm occurrence are advected in the atmosphere. A fit to the data provides $c = 5.2(3) \text{ m s}^{-1}$, which is similar to typical low- to mid-tropospheric wind speeds in Central Europe. Lines of constant spatial scale appear as dashed lines in fig. 8. Classification skill increases with s . This is consistent with the work of Roberts (2008), which investigates the spatial variation of precipitation forecast skill.

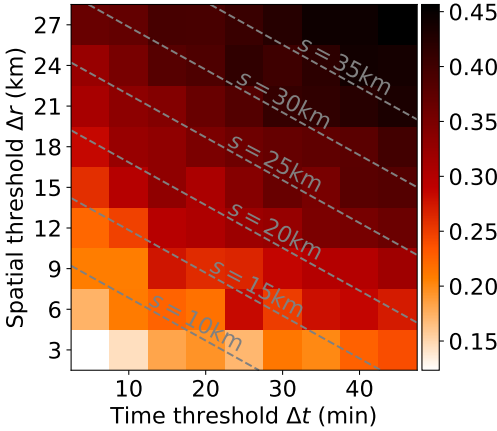


FIGURE 8 (Color online) Classification skill of SALAMA, expressed in terms of the area under the PR curve, as a function of the label configuration (cf. section 2.2). The slope of the dashed lines is chosen such that classification skill is approximately constant along the lines. Each line corresponds to a specific spatial scale s (cf. eq. (13)).

Next, we investigate how the decrease of classification skill with lead time depends on the spatial scale. Motivated by the observed decay of classification skill with lead time (cf. section 4.2), we fit an exponential function $\exp(-t_{\text{lead}}/\tau)$ to the lead time dependence of classification skill (measured again by the area under the PR curve). The skill decay time τ then provides a characteristic time scale for the decrease of classification skill. For each label configuration in fig. 8, we compute the corresponding spatial scale as well as τ . In fig. 9, we present a scatter plot of τ and s . The figure shows a tight positive linear correlation between the two quantities, which means that classification skill decreases more slowly for coarser label configurations. This is in agreement with the anticipation (Lorenz, 1969) that the ability to resolve smaller scales in NWP models results in forecast errors growing more rapidly. Our finding is complementary to convection studies involving a scale-dependent skill score (Roberts, 2008), and high-resolution simulations (Selz and Craig, 2015).

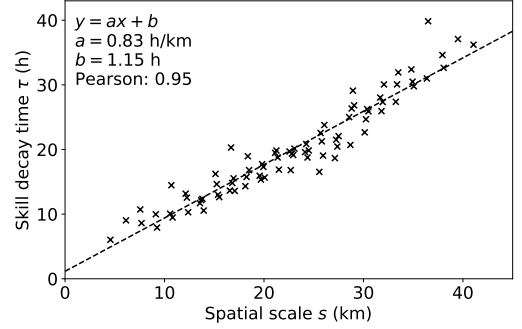


FIGURE 9 Decay time of classification skill (quantified by the area under the PR curve) as a function of the spatial scale. Each data point corresponds to one label configuration in fig. 8. The parameters of a linear fit are also shown, as well as the Pearson coefficient of correlation.

5 | CONCLUSION AND PERSPECTIVES

Addressing the need for accurate thunderstorm forecasting and leveraging advances in high-resolution NWP and ML, we have presented SALAMA, a feedforward neural network model that identifies thunderstorm occurrence in NWP forecasts up to 11 h in advance in a pixel-wise manner. The inference of the probability of thunderstorm occurrence is based on input parameters that are physically related to thunderstorm activity and do not explicitly feature information on location, time or forecast range. This gives reason to expect that the signature learned by the model generalizes to thunderstorms outside the study region of this work and remains valid in a changing climate. In addition, the availability of all input features in real time makes SALAMA readily available for operational use.

We have addressed the technical challenge caused by the rarity of thunderstorms and the corresponding small fraction of positive examples by increasing this fraction during training and analytically accounting for the increase when testing. This approach has allowed us to ensure reasonable reliability without calibration fits. We have argued that including a further calibration step would not affect the performance results of SALAMA.

Working with ensemble data, we have studied how the NWP forecast uncertainty depends on the lead time of the

forecast and related it to the classification skill decrease of SALAMA. This has suggested that the decrease in skill is the result of an increasing uncertainty in the input feature forecasting.

During the training process, we have systematically varied the spatiotemporal criteria by which we associate lightning observations with NWP data. This has allowed us to test SALAMA with different spatial scales and to estimate the order of magnitude of the speed at which thunderstorms are advected in the atmosphere. We have shown that classification skill (quantified by the area under the precision-recall curve) increases with the spatial scale of the forecast and is higher than for a baseline model based on CAPE alone. Furthermore, we have found that the decay time of classification skill is proportional to the spatial scale. In combination with the result that the SALAMA classification skill is correlated with the NWP forecast uncertainty, our findings have indicated that resolving thunderstorms at smaller scales reduces the predictability of thunderstorm occurrence.

In a future work, it is useful to check the universality of the thunderstorm signature learned by SALAMA, e.g. by testing it on data outside of Central Europe or for a different time period than the summer of 2021. Moreover, one may explore whether classification skill can be improved by shifting from a pixel-wise consideration of input features to taking their spatiotemporal structure into account as well.

6 | AUTHOR CONTRIBUTIONS

K. Vahid Yousefnia: Methodology; software; investigation; resources; visualization; writing - original draft; writing - review and editing. **T. Bölle:** Conceptualization; writing - review and editing. **I. Zöbisch:** Conceptualization; resources; writing - review and editing. **T. Gerz:** Writing - review and editing; supervision.

7 | DATA AVAILABILITY

The Python code for SALAMA will be made available upon reasonable request.

8 | ACKNOWLEDGEMENTS

We thank George Craig and Tobias Selz for helpful discussions. This work was funded through the internal project DIAL of the German Aerospace Center (DLR). We gratefully acknowledge the computational and data resources provided through the joint high-performance data analytics (HPDA) project "terabyte" of the DLR and the Leibniz Supercomputing Center (LRZ). The authors declare that there are no conflicts of interest to disclose.

REFERENCES

- Bauer, P., Thorpe, A. and Brunet, G. (2015) The quiet revolution of numerical weather prediction. *Nature*, **525**, 47–55.
- Betz, H. D., Schmidt, K., Laroche, P., Blanchet, P., Oettinger, W. P., Defer, E., Dzierwit, Z. and Konarski, J. (2009) Linet—an international lightning detection network in europe. *Atmospheric Research*, **91**, 564–573. 13th International Conference on Atmospheric Electricity.
- Borsky, S. and Unterberger, C. (2019) Bad weather and flight delays: The impact of sudden and slow onset weather events. *Economics of Transportation*, **18**, 10–26. URL: <https://www.sciencedirect.com/science/article/pii/S2212012218300753>.
- Bröcker, J. and Smith, L. A. (2007) Increasing the reliability of reliability diagrams. *Weather and Forecasting*, **22**, 651–661. URL: https://journals.ametsoc.org/view/journals/wefo/22/3/waf993_1.xml.
- Diffenbaugh, N. S., Scherer, M. and Trapp, R. J. (2013) Robust increases in severe thunderstorm environments in response to greenhouse forcing. *Proceedings of the National Academy of Sciences*, **110**, 16361–16366. URL: <https://www.pnas.org/doi/abs/10.1073/pnas.1307758110>.
- Geng, Y.-a., Li, Q., Lin, T., Yao, W., Xu, L., Zheng, D., Zhou, X., Zheng, L., Lyu, W. and Zhang, Y. (2021) A deep learning framework for lightning forecasting with multi-source spatiotemporal data. *Quarterly Journal of the Royal Meteorological Society*, **147**, 4048–4062. URL: <https://rmets.onlinelibrary.wiley.com/doi/abs/10.1002/qj.4167>.
- Gerz, T., Forster, C. and Tafferner, A. (2012) *Mitigating the Impact of Adverse Weather on Aviation*, 645–659. Berlin, Heidelberg: Springer Berlin Heidelberg. URL: https://doi.org/10.1007/978-3-642-30183-4_39.

- Holle, R. L. (2014) Some aspects of global lightning impacts. In *2014 International Conference on Lightning Protection (ICLP)*, 1390–1395.
- (2016) A summary of recent national-scale lightning fatality studies. *Weather, Climate, and Society*, **8**, 35 – 42. URL: https://journals.ametsoc.org/view/journals/wcas/8/1/wcas-d-15-0032_1.xml.
- Hwang, Y., Clark, A. J., Lakshmanan, V. and Koch, S. E. (2015) Improved nowcasts by blending extrapolation and model forecasts. *Weather and Forecasting*, **30**, 1201 – 1217. URL: https://journals.ametsoc.org/view/journals/wefo/30/5/waf-d-15-0057_1.xml.
- Jardines, A., Soler, M., Cervantes, A., García-Heras, J. and Simarro, J. (2021) Convection indicator for pre-tactical air traffic flow management using neural networks. *Machine Learning with Applications*, **5**, 100053. URL: <https://www.sciencedirect.com/science/article/pii/S2666827021000256>.
- Kamangir, H., Collins, W., Tissot, P. and King, S. A. (2020) A deep-learning model to predict thunderstorms within 400 km² south texas domains. *Meteorological Applications*, **27**, e1905. URL: <https://rmets.onlinelibrary.wiley.com/doi/abs/10.1002/met.1905>.
- Kingma, D. P. and Ba, J. (2014) Adam: A method for stochastic optimization. URL: <https://arxiv.org/abs/1412.6980>.
- Kober, K., Craig, G. C., Keil, C. and Dörnbrack, A. (2012) Blending a probabilistic nowcasting method with a high-resolution numerical weather prediction ensemble for convective precipitation forecasts. *Quarterly Journal of the Royal Meteorological Society*, **138**, 755–768. URL: <https://rmets.onlinelibrary.wiley.com/doi/abs/10.1002/qj.939>.
- Leinonen, J., Hamann, U., Germann, U. and Mecikalski, J. R. (2022) Nowcasting thunderstorm hazards using machine learning: the impact of data sources on performance. *Natural Hazards and Earth System Sciences*, **22**, 577–597. URL: <https://nhess.copernicus.org/articles/22/577/2022/>.
- Li, J., Forster, C., Wagner, J. and Gerz, T. (2021) Cb-fusion-forecasting thunderstorm cells up to 6 hours. *Meteorologische Zeitschrift*, 169–184.
- Lin, P.-F., Chang, P.-L., Jou, B. J.-D., Wilson, J. W. and Roberts, R. D. (2012) Objective prediction of warm season afternoon thunderstorms in northern taiwan using a fuzzy logic approach. *Weather and Forecasting*, **27**, 1178 – 1197. URL: https://journals.ametsoc.org/view/journals/wefo/27/5/waf-d-11-00105_1.xml.
- Lorenz, E. N. (1969) The predictability of a flow which possesses many scales of motion. *Tellus*, **21**, 289–307. URL: <https://doi.org/10.3402/tellusa.v21i3.10086>.
- Markowski, P. and Richardson, Y. (2011) *Mesoscale meteorology in midlatitudes*. John Wiley & Sons.
- Niculescu-Mizil, A. and Caruana, R. (2005) Predicting good probabilities with supervised learning. In *Proceedings of the 22nd International Conference on Machine Learning, ICML '05*, 625–632. New York, NY, USA: Association for Computing Machinery. URL: <https://doi.org/10.1145/1102351.1102430>.
- Rädler, A. T., Groenemeijer, P. H., Faust, E., Sausen, R. and Púčik, T. (2019) Frequency of severe thunderstorms across europe expected to increase in the 21st century due to rising instability. *npj Climate and Atmospheric Science*, **2**, 30.
- Reinert, D., Prill, F., Frank, H., Denhard, M., Baldauf, M., Schraff, C., Gebhardt, C., Marsigli, C. and Zängl, G. (2020) Dwd database reference for the global and regional icon and icon-eps forecasting system. *Technical report Version 2.1. 8*, Deutscher Wetterdienst. URL: https://www.dwd.de/DWD/forschung/nwv/fepub/icon_database_main.pdf.
- Roberts, N. (2008) Assessing the spatial and temporal variation in the skill of precipitation forecasts from an nwp model. *Meteorological Applications*, **15**, 163–169. URL: <https://rmets.onlinelibrary.wiley.com/doi/abs/10.1002/met.57>.
- Selz, T. and Craig, G. C. (2015) Upscale error growth in a high-resolution simulation of a summertime weather event over europe. *Monthly Weather Review*, **143**, 813 – 827. URL: <https://journals.ametsoc.org/view/journals/mwre/143/3/mwr-d-14-00140.1.xml>.
- Sun, J., Xue, M., Wilson, J. W., Zawadzki, I., Ballard, S. P., Onvlee-Hooimeyer, J., Joe, P., Barker, D. M., Li, P.-W., Golding, B., Xu, M. and Pinto, J. (2014) Use of nwp for nowcasting convective precipitation: Recent progress and challenges. *Bulletin of the American Meteorological Society*, **95**, 409 – 426. URL: <https://journals.ametsoc.org/view/journals/bams/95/3/bams-d-11-00263.1.xml>.
- Ukkonen, P. and Mäkelä, A. (2019) Evaluation of machine learning classifiers for predicting deep convection. *Journal of Advances in Modeling Earth Systems*, **11**, 1784–1802. URL: <https://agupubs.onlinelibrary.wiley.com/doi/abs/10.1029/2018MS001561>.
- Veraverbeke, S., Rogers, B. M., Goulden, M. L., Jandt, R. R., Miller, C. E., Wiggins, E. B. and Randerson, J. T. (2017) Lightning as a major driver of recent large fire years in north american boreal forests. *Nature Climate Change*, **7**, 529–534.

- Yano, J.-I., Ziemiański, M. Z., Cullen, M., Termonia, P., On-
vlee, J., Bengtsson, L., Carrassi, A., Davy, R., Deluca,
A., Gray, S. L., Homar, V., Köhler, M., Krichak, S.,
Michaelides, S., Phillips, V. T. J., Soares, P. M. M.
and Wyszogrodski, A. A. (2018) Scientific challenges of
convective-scale numerical weather prediction. *Bulletin
of the American Meteorological Society*, **99**, 699 – 710.
URL: [https://journals.ametsoc.org/view/journals/
bams/99/4/bams-d-17-0125.1.xml](https://journals.ametsoc.org/view/journals/bams/99/4/bams-d-17-0125.1.xml).
- Yasuda, Y., Yokoyama, S., Minowa, M. and Satoh, T. (2012)
Classification of lightning damage to wind turbine blades.
IEEE Transactions on Electrical and Electronic Engineering,
7, 559–566. URL: [https://onlinelibrary.wiley.com/
doi/abs/10.1002/tee.21773](https://onlinelibrary.wiley.com/doi/abs/10.1002/tee.21773).
- Zhou, K., Sun, J., Zheng, Y. and Zhang, Y. (2022) Quantitative
precipitation forecast experiment based on basic nwp vari-
ables using deep learning. *Advances in Atmospheric Sci-
ences*, **39**, 1472–1486.
- Zöbisch, I., Forster, C., Zinner, T., Bugliaro, L., Tafferner, A.
and Wapler, K. (2020) Characteristics of deep moist con-
vection over germany in multi-source data. *Meteorologis-
che Zeitschrift*, **29**, 393–407. URL: [http://dx.doi.org/
10.1127/metz/2020/1011](http://dx.doi.org/10.1127/metz/2020/1011).
- Zängl, G., Reinert, D., Rípodas, P. and Baldauf, M. (2015) The
icon (icosahedral non-hydrostatic) modelling framework of
dwd and mpi-m: Description of the non-hydrostatic dynami-
cal core. *Quarterly Journal of the Royal Meteorological Soci-
ety*, **141**, 563–579. URL: [https://rmets.onlinelibrary.
wiley.com/doi/abs/10.1002/qj.2378](https://rmets.onlinelibrary.wiley.com/doi/abs/10.1002/qj.2378).